IOP Publishing Journal of Physics: Condensed Matter
J. Phys.: Condens. Matter **32** (2020) 185703 (7pp) https://doi.org/10.1088/1361-648X/ab6b8a

Strain-controlled ferromagnetism in $BiFeO_3$ nanoparticles

E Ramos[1], A Cardona-Rodríguez[1], D Carranza-Celis[1], R González-Hernández[2], D Muraca[3] and Juan Gabriel Ramírez[1]

[1] Department of Physics, Universidad de los Andes, Bogotá 111711, Colombia
[2] Grupo de Investigación en Física Aplicada, Departamento de Física, Universidad del Norte, Barranquilla, Colombia
[3] Instituto de Física 'Gleb Wataghin', Universidade Estadual de Campinas (UNICAMP), CEP13083-859 Campinas, São Paulo, Brazil

E-mail: jgramirez@uniandes.edu.co

Received 6 September 2019, revised 18 December 2019
Accepted for publication 14 January 2020
Published 4 February 2020

Abstract

Multiferroic materials are at the core of voltage-controlled spintronic devices. Therefore, an understanding of the underlying electronic correlations and their effects associated with their complex energy landscape is an important and ongoing task. One key parameter in oxide-based perovskite multiferroics is their sensitivity to strain effects under confinement. Here, we report on the ferromagnetism induced by strain-engineering at the nanoscale on $BiFeO_3$ (BFO) nanoparticles. By controlling synthesis parameters, we were able to modify the BFO lattice parameters up to 0.15% and as a consequence, induce ferromagnetism in otherwise antiferromagnetic bulk BFO. In order to understand the driving mechanisms behind such an effect, we performed density functional theory calculations (DFT) using the BFO parameters obtained from the experiment. We found that small distortions of the structural lattice parameters of the order of 0.01% are sufficient to induce a significant spin imbalance close to the Fermi energy at the Fe sites. This may explain the appearance of weak ferromagnetism in strained BFO thin films reported earlier and offers a new route to novel voltage-controlled spintronic devices based on multiferroic materials.

Keywords: multiferroic, nanoparticles, density functional theory

S Supplementary material for this article is available online

(Some figures may appear in colour only in the online journal)

1. Introduction

Oxide perovskites provide an increasingly-interesting playground for new physic and applications. This is due to the complex interactions that allow for the coupling of magnetic and electronic degrees of freedom [1]. In these systems, a slightly offset of the stoichiometric oxygen content can produce significant changes in the crystal lattice parameters as well as the overall macroscopic properties. Furthermore, lattice strain can induce new magnetic phases or change the electronic response dramatically. Therefore, the strain is an ideal tuning parameter to investigate the underlying physics in these materials [2].

Controlling strain on a material is usually done during the synthesis of bulk crystals (intrinsic) through controlling the fabrication temperature, chemical doping, or by controlling external stimuli such as pressure [3–5]. Inducing strain during the synthesis process without the use of any chemical dopants allows for access to other thermodynamically stable states of the crystal structure, and therefore helps maintain the overall properties of the material. For example, crystals that are forced to grow in nanoparticle form tend to exhibit a contraction in crystal lattice parameters thus reducing the volume. This is particularly interesting in nanoparticles of oxide perovskites with short-range interactions, where new band gaps may appear by confinement effects [6]. Multiferroic materials

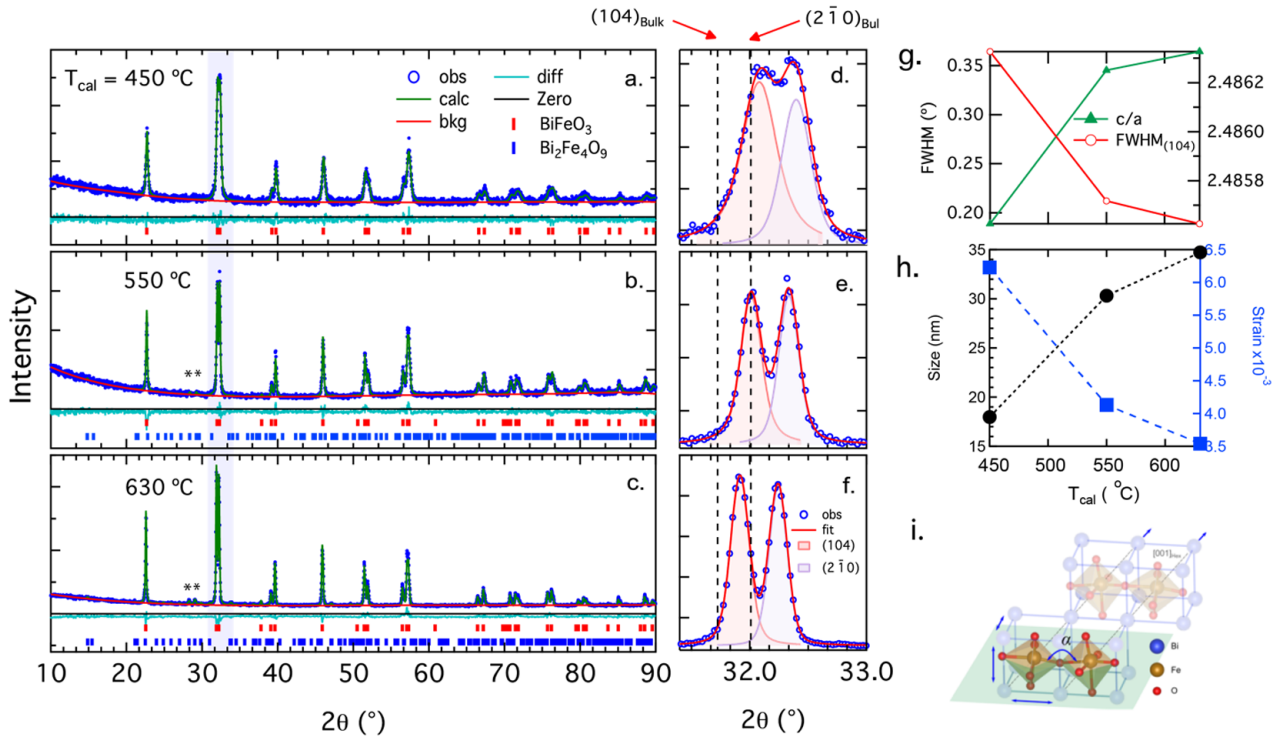

Figure 1. Room temperature XRD of BFO nanoparticles calcinated at different temperatures. (a) 450 °C, (b) 550 °C, (c) 630 °C. The observed data, the Rietveld refinement, the obtained background and difference are all plotted. We have added the Bragg planes of the main and secondary phases for reference. The matching peaks of the secondary phases are indicated by the symbol (∗). The (1 0 4) and (2 − 1 0) planes for each T_{cal} is presented in (d) and (e). Vertical dashed lines indicate the bulk reference values for both reflections. The red line corresponds to a fitting with two Voight functions. Individual contributions are plotted as a reference. From these, FWHM and peak positions were obtained. In (g) we plot the FWHM of the plane (1 0 4) and the c/a ratio as a function of T_{cal}. (h) Shows the plot of the strain, and also the crystallite size obtained based on a modified Williamson–Hall method (see supplemental material). In (i) we depict the refined BFO unit cell (R3cH). We indicate the Fe–O–Fe bond-angle α.

are such an example where the magnetic and electric degrees of freedom are strongly coupled [7–9].

There are only a few single-phase magnetoelectric (ME) materials at room temperature. One of them is the bismuth ferrite, $BiFeO_3$ (BFO) [10]. BFO is an archetypical ferroelectric multifunctional oxide with rhombohedral distorted perovskite structure that belongs to the R3c space group. BFO displays a Dzyaloshinskii–Moriya (DM) interaction among nearest neighbor Fe^{3+} spins [11–13] that produces an antiferromagnetic long-cycloid spin structure with a wavelength of 62 nm [14] reported in bulk. In addition, DM interaction is responsible for ME coupling [15]. BFO has a high Néel temperature (640 K) and high a Curie transition temperature (1100 K), as well as high polarization of Ps = ~100 μC cm^{-2} in the [1 1 1] crystallographic direction. Both bulk BFO and thin film BFO are known for exhibiting a strong ME coupling effect which gives rise to multiple industrial applications [7, 9, 13, 16, 17]. Furthermore, due to the long-cycloid spin structure of BFO caused by the DM interaction [14, 18], there is a residual ferromagnetic response at room temperature which suggests the possibility of turning BFO into a multiferroic material with both magnetic and electric ferroic orders using nanostructuration in the form of nanoparticles [19, 20] or ultra-thin films [10, 21]. However, the exact mechanism that drives the magnetic order is not known. Recently, attempts to explain the spin imbalance using density functional theory (DFT) calculations have been done using the bulk structures [5, 22], strained thin films [5], and also at the interface of ferromagnetic materials [23]. The results suggest that the canting of the magnetic sublattices is caused by the DM spin coupling due to the combined action of the exchange interaction and spin–orbit coupling which is controlled by strain in the crystal structures via oxygen tilting with respect to the Fe atoms.

In this paper, we report on the magnetic properties of $BiFeO_3$ nanoparticles in which we have systematically varied the growth conditions to induce a structural strain. We have calculated the strain via x-ray diffraction (XRD) data and high-resolution transmission electron microscopy (TEM) measurements. We have found that in smaller particles, the lattice is strained by a factor between 0.15% and 0.18% with respect to the bulk. In contrast, the strain diminishes in the bigger particles, with lattice values approaching those of bulk BFO. Furthermore, the NPs magnetic moment decreases with decreasing lattice strain. In order to account for the appearance and the scaling of the magnetic moment with strain, we performed first-principles calculations in the framework of DFT using the XRD refined structures. We found that even small changes in the lattice due to strain can induce a significant spin imbalance close to the Fermi level and therefore produce a net magnetic moment even without spin–orbit coupling interactions. Furthermore, the calculated magnetic moment decreases with the strain as in the experiments. Our results demonstrate a clear pathway to control the magnetic response

in BFO NPs using strain engineering, which will open new routes for nanoscale spintronics devices.

2. Methods

In order to obtain BFO NPs we prepared the xerogel powder following the same method described in [24]. This final gel was calcined for 3 h in an oven at temperatures (T_{cal}) 450 °C, 550 °C and 630 °C. Finally, the resulting powder was washed out several times with deionized water and glacial acetic acid and subsequently let to dry at room temperature. The crystal structure of the powder was determined by XRD. We used Cu-k_α radiation over an angular range of 2θ from 5 to 90 degrees with a step size of 0.002 degrees in order to perform a meaningful Rietveld refinement using the Profex software [25]. Typical Raman resonant modes of BFO R3c were confirmed. The local structure was characterized by TEM using a JEOL TEM-FEG (JEM 2100F, 300 KV) and JEOL TEM-MSC (JEM 2100, 200 KV). The images were acquired using a Gatan/Orius SC600/831 camera at different magnifications and analyzed using Gatan Micrograph software. The samples were prepared before the experiment by drying a drop of a dispersion over ultrathin carbon film supported on holey carbon (Ted Pella). The magnetization hysteresis curves (M versus H) at room temperature were obtained with a Lakeshore™ vibrating sample magnetometer (VSM).

First-principles calculations were performed within the framework of DFT using the Vienna *ab initio* simulation package (VASP) [26]. The Kohn-Sham equations were solved self-consistently using the pseudopotential plane-wave method. We have employed the generalized gradient approximation method plus the Hubbard U correction (GGA + U) approach [27]. The electron wave functions were expanded in plane waves up to a cut-off energy of 500 eV and a grid of $44 \times 44 \times 44$ k-point has been used to sample the irreducible Brillouin zone. In addition, we used the refined structural parameters extracted from the experimental XRD data as an input for our DFT calculations. Spin and charge densities within the unit cell was also calculated in order to map the changes induced by strain.

3. Results

In figure 1 we show the XRD at room temperature of the prepared BFO NPs. Figure 1(a) corresponds to the NPs calcined (T_{cal}) to 450 °C, 550 °C and 630 °C (blue open circle). Single-phase BFO powder was obtained as demonstrated by the absence of additional Bragg peaks. In order to extract the crystal symmetries and lattice parameters, we have performed a Rietveld analysis of the measured data. We have included the $BiFeO_3$ and $Bi_2Fe_4O_9$ phases in the refinement (ICSD: R3cH-15299, Pbam-20067) and found a good match with a χ^2 of 1.15, 1.20 and 1.41 for 450 °C, 550 °C and 630 °C respectively (figures 1(a)–(c)). The green continuous line depicts the fitting results. Interestingly, we have found that as T_{cal} decreases (i) there is a trend for the (1 0 4) and (2 − 1 0) peaks to shift at higher angles and (ii) the full width at high

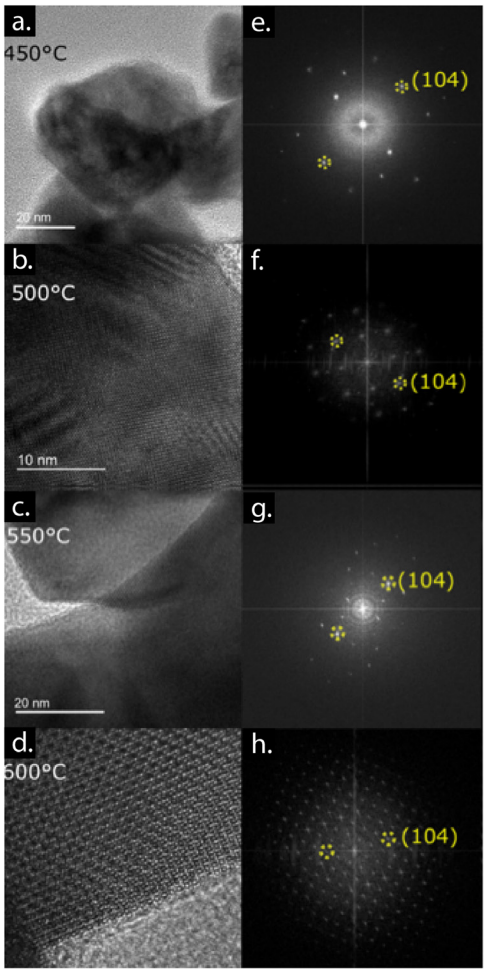

Figure 2. TEM images for BFO NPs calcinated at different T_{cal} (a)–(d), and their respective FFT (e)–(h) where the (1 0 4) plane is highlighted.

maximum (FWHM) increases in each peak. The former indicates a reduction of the unit cell as captured by the Rietveld refinement, and the latter suggests a decrease of particle size as T_{cal} decreases. We fitted the individual (1 0 4) and (2 − 1 0) peaks with Voight functions for all temperatures. Individual contributions from each reflection are plotted in figures 1(d)–(f). To compare it with the BFO bulk reference data, we added a vertical dashed line at the (1 0 4) and (2 − 1 0) planes to which we compare our NPs indicated. In figure 1(d) we obtained the lattice spacing of each reflection which were plotted for each T_{cal}. Again, a reduction of the d spacing is found with increasing T_{cal}. Furthermore, the c/a ratio also increases as well with increasing T_{cal} (see figure 1(g)).

The reduction of the unit cell with decreasing T_{cal} points to an increase of strain in the lattice. We, therefore, calculated the strain by performing a modified version of the Williamson–Hall plot using the FWHM for each Bragg Reflection assuming a isotropic line broadening. The details of the procedure are in the supplemental material (stacks.iop.org/JPhysCM/32/185703/mmedia). In figure 1(h) we plot the obtained microstrain as a function of $T_{cal.}$ It is possible to also obtain the crystallite size as well from the same method, provided all the sources of the broadening of the peak width are

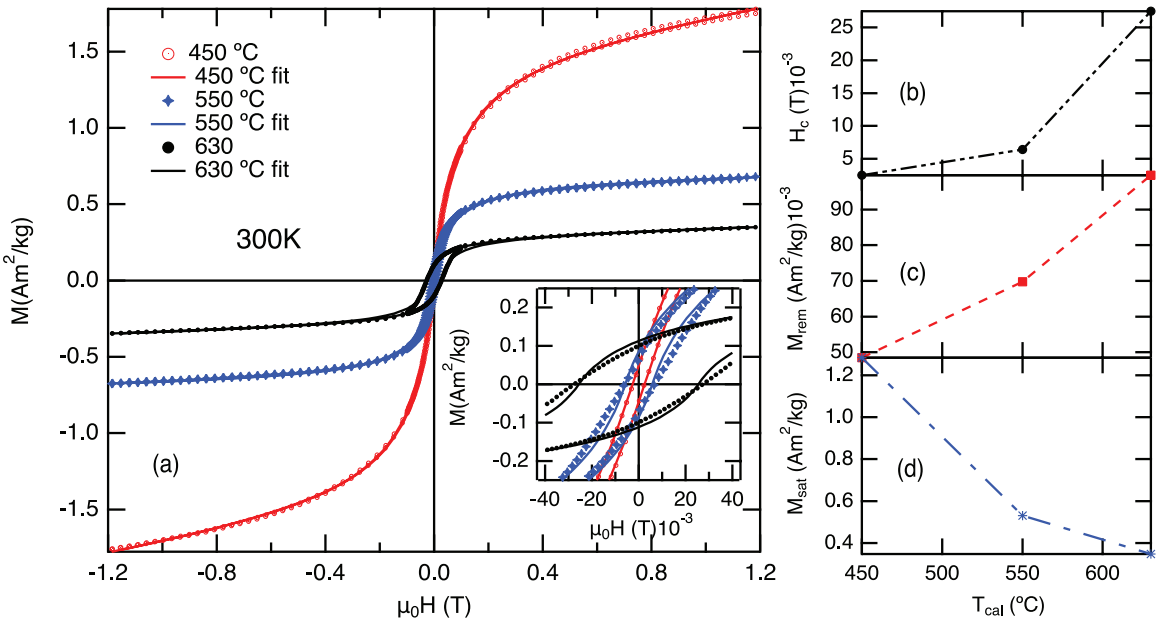

Figure 3. Magnetization curves as a function of the magnetic field for BFO NPs synthesized at 450 °C, 550 °C, and 630 °C. The inset is a zoom in the coercivity region for the three different temperatures T_{cal} and the global magnetic properties as (b) coercivity, (c) remanence magnetization and (d) magnetization of saturation respectively.

known [28]. In figure 1(h) we plot the obtained size as a function of T_{cal}. Both, the crystallite size and the microstrain are negatively correlated thus corroborating observations (i) and (ii) listed above. Figure 1(i) depicts the refined crystal structure with the R3c symmetry.

Since XRD measurements are a macroscopic representation of the sample, we performed TEM measurements in order to obtain the local lattice parameters inside our particles. In figure 2 we show the high-resolution TEM images and the corresponding FFT where the (1 0 4) plane is highlighted. Note that these measurements correspond to a bigger set of samples with a broader calcination temperature value. We observed in all TEM images a set of diffraction planes solely arising from BFO R3c symmetry, thus indicating that the particles are single-phase BFO with a high degree of crystallinity. Since the (1 0 4) reflection corresponds to the more intense Bragg peak, we have chosen it to gain knowledge of the special distribution of the rhombohedral BFO phase inside the particles. This is motivated by other studies in oxide particles that describe a core-shell structure of intrinsic crystallographic phases [29]. We found a homogeneous distribution of the (1 0 4) lattice planes (not shown) and therefore we conclude that the lattice structure obtained by the XRD data is representative of a single particle as well.

The magnetic response of the BFO NPs as a function of the T_{cal} is depicted in figure 3. In figure 3(a) we show the isothermal hysteresis loops of BFO NPs at room temperature. We identify a crossover between a ferromagnetic-like behavior at higher T_{cal} and a superparamagnetic-like behavior at lower T_{cal}. The hysteresis loops were fitted employing a Langevin equation with a coercive field dependence and a lognormal-type distribution of magnetic moments assuming a modified superparamagnetic-particle model in order to extract the saturation magnetization, remanence, and coercive field. These parameters show a superparamagnetic tendency for T_{cal} 450 °C. Figures 3(b) and (c) and a ferromagnetic-like behavior for 550 °C and 630 °C. These results are in agreement with ferrogel nanoparticles [30].

4. Discussion

We have found a ferromagnetic-like response in our NPs that appears to be negatively correlated in magnitude to the among of microstrain as calculated from our XRD measurements and corroborated by the TEM measurements. This result suggests that the changes in the atomic arrangement modify the magnetoelectric (spin-lattice) coupling known to exist in BFO [11]. For example, from the refined structures, we found an increase of the Fe–O–Fe angle, which is fundamental for the magnetic coupling of Fe atoms, since it gives rise to the DM coupling in BFO and gives origin to the spin cycloid [31]. Therefore, it remains unclear if the induced magnetic response in our NPs is due to a change in the DM coupling (since unpaired spins may appear in NPs with smaller sizes compared to the reported spin cycloid for bulk BFO (62 nm)), or if the magnetic response observed is a consequence of the microstrain alone.

To investigate this further, we performed first principle calculations using the projector-augmented wave (PAW) method [32] within the spin-density generalized gradient approximation plus the on-site repulsion (GGA + U), as implemented in the VASP software [32]. We included the spin–orbit coupling in our calculations and found no significant change in the magnetic properties reported (see figures S1(b) and (c)). This follows from the relative population of states in the valence band where the upper states consist of more p-O states and less s-Bi states. These p-O orbitals show a weak SOC. Therefore, SOC is not an imperative effect in BFO and was left out from the following calculations.

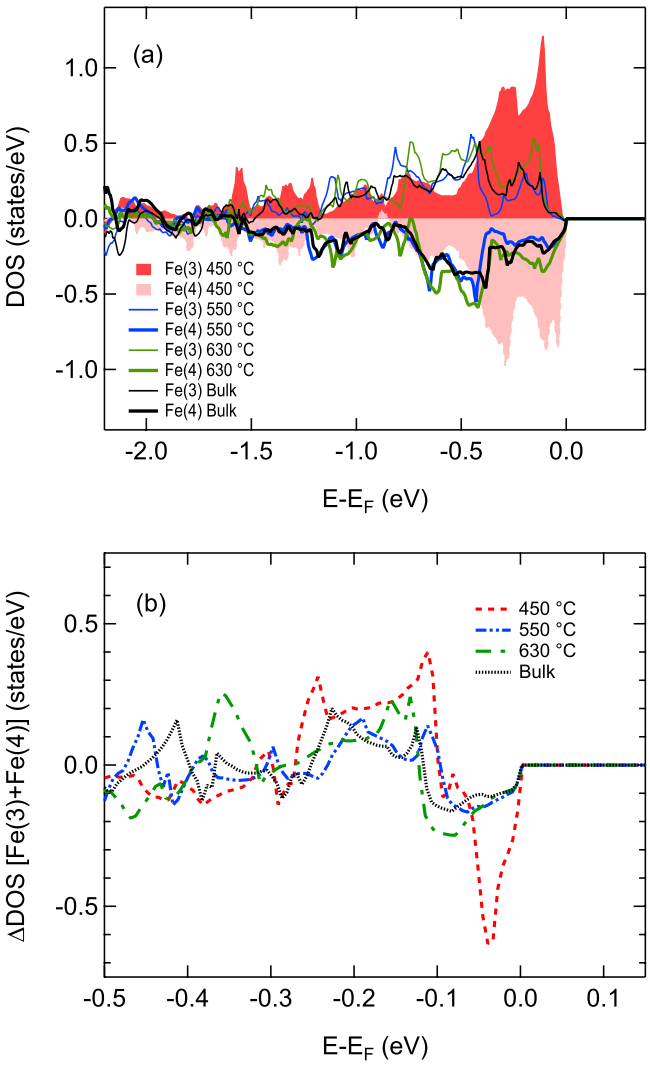

Figure 4. (a) Calculated DOS for d-orbitals of Fe atoms (Fe(3)-up and Fe(4)-down) BFO single cell as a function of the relative energy spectrum. Input parameters are taken from the experiment for each calcination temperature. (b) DOS spin difference for Fe atoms to highlight the increase of the spin imbalance near the Fermi energy.

We have used the refined structures for our calculations and therefore no crystal relaxation was performed in our DFT calculations. By using the refined structures in our DFT, we are taking into account only the effects due to microstrain. It is important to note that other effects intrinsic to the NPs are not accounted for, like surface effects and possible particle-to-particle interactions.

In our simulations, the antiferromagnetic axis was left free to relax but initially set to the [1 1 1] direction in the rhombohedral crystal structure and no DM interaction was included. The calculations were performed with 15 × 15 × 15 *k*-point sampling. Additional calculations were done with 29 × 29 × 29 and 44 × 44 × 44 grids and found no significant differences in the results.

In figure 4 we summarize our DFT results. The spin up and down density of states (DOS) of the Fe atoms in the unit cell is plotted for all the structures calculated, as a function of the energy relative to the Fermi level. Fe(3) and Fe(4) are illustrated in figure 1(h) and in figure S1(a), respectively. The full calculation includes a broader energy range as depicted in figure S2. As a reference, we have performed the same calculations in a reference bulk structure with similar R3c structure (black thick line in figure 4). We see a decrease of the DOS for the Fe atom (spin up and down) with increasing T_{cal}. Interestingly, we do observe a small spin imbalance in all structures calculated. This imbalance is energy-dependent and robust with the DFT parameters. Therefore, it is possible to obtain a small ferromagnetic behavior even in bulk samples, and results in this direction have also been reported in thin-film structures [33, 34]. Our calculations are in agreement with other first principle calculations performed for bulk structures [35] and thin films [36, 37] where relaxation of the crystal structure was performed. In order to account for the asymmetry of the spin up and down DOS we subtracted the up and down DOS. Figure 4(b) shows the DOS close to the Fermi energy level. It is clear that the sample which was calcined to 450 °C has the highest difference in DOS. This implies that it should have a higher magnetic moment per unit cell. This is corroborated by the results from our experiment as depicted in figure 3(d). Therefore, our DFT results suggest that the principal contribution to the appearance of weak ferromagnetism that fades out as strain is relieved in our NPs during the synthesis process. We can investigate further the distribution of the excess spin density in the real space by calculating the total spin-charge density.

Figure 5 shows our calculations for all the structures analyzed. In figure 5(d) we show as a reference, the 2D density plot of the total spin density within the BFO unit cell of a reference BFO bulk structure. We have indicated the Fe(3) and Fe(4) atoms that have an opposite spin (with spin up and down corresponding to red and blue colors, respectively) and therefore conserving an antiferromagnetically-coupled structure. The vertical axis corresponds to the [0 1 0] direction in the vertical axis and the [1 0 − 1] direction is along the horizontal axis. We constructed similar plots for all structures and calculated the difference using the BFO bulk as a reference as shown in figures 5(a)–(c). We observe that the changes in the spin density are non-depreciable in all cases as can be noticed by the intensity scales. The main contribution to the increase comes from local variations in the spin density around the Fe–O–Fe bonds as depicted in the dashed-line box in figure 5(a). Therefore, the change in the Fe–O–Fe angle is a crucial parameter for manipulating the magnetic properties of BFO NPs.

Since BFO has a considerable magnetoelectric effect when nanostructured, as reported in thin films [38], we performed DFT calculations of the charge density displacement for all BFO samples. Similar to the spin density calculations discussed above, we obtained the charge distribution within the unit cell for a bulk sample as shown in figure 5(i). Interestingly, we observed an overall redistribution of charge within the unit cell as compared to the bulk. The redistribution of charge occurs around the Fe atoms and from variations around the O atoms due to the oxygen displacements in the strained cell. Both effects, the redistribution of charge and of spin in our

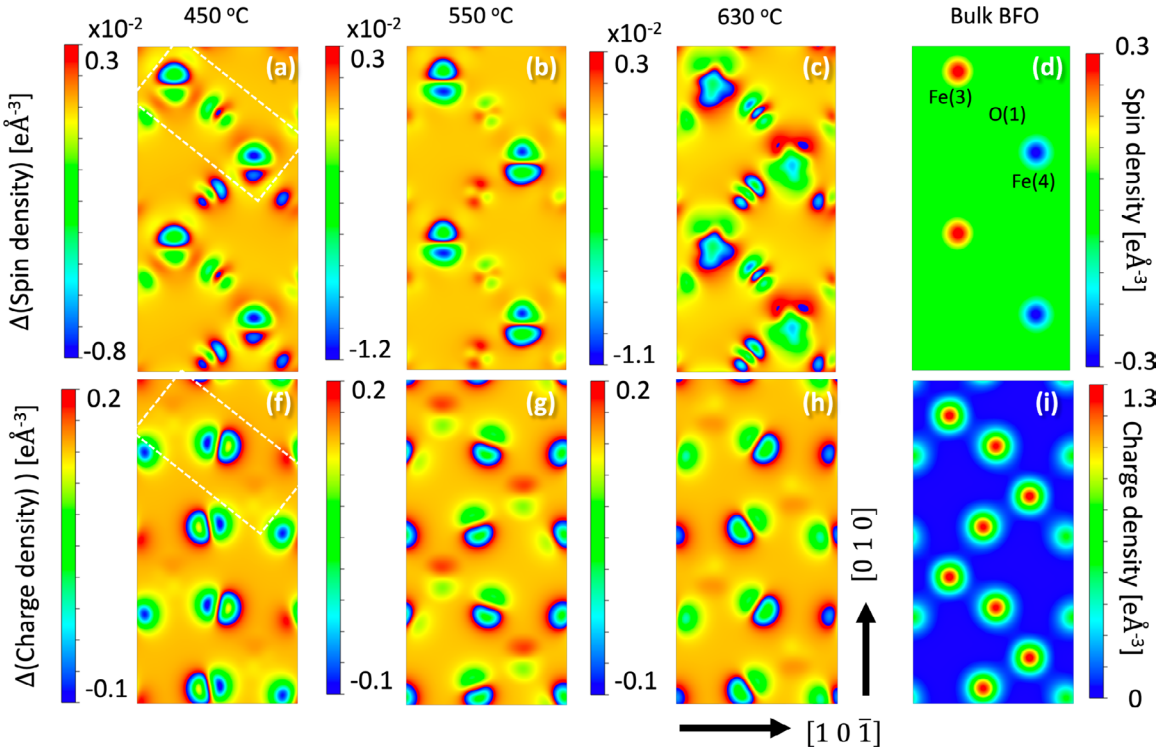

Figure 5. Calculated electronic spin-charge difference for 450 °C (a), 550 °C (b) and 630 °C (c) in the plane (2, −1, 0) respect to BFO in bulk (d). In (a)–(c) the color map corresponds to the changes in spin density when subtracted to BFO bulk. In (d) the color map represents the spin density, where red and blue corresponds to spin-up and spin-down electrons, respectively. Similarly, bottom panel indicates changes in the charge density (f)–(h) with respect to BFO bulk, and in (i) the color map represents the charge density alone, where red and blue indicates high and low electronic charge density, respectively. Charge difference for 450 °C (f), 550 °C (g) and 630 °C (h) respect to BFO in bulk (i). Boxes highlight the Fe(3), Fe(4) and O(1) atoms in the unit cell. The spin and charge densities where calculated using VASP code. Details of the procedure in supplemental material.

BFO NPs suggest that global properties that depend upon those quantities should also exhibit a change. For example, as shown in figure S3 (i) the calculated charge and spin density are anticorrelated, (ii) the electronic gap increases and (iii) the crystal energy decreases, all with decreasing strain (increasing T_{cal}). Therefore, investigating the magnetoelectric effect in strained BFO NPs may allow for strong coupling of spin and charge. Measuring the magnetoelectric effect is out of the scope of this paper.

5. Conclusions

We report on the ferromagnetism induced by strain-engineering at the nanoscale on $BiFeO_3$ (BFO) nanoparticles by controlling the calcination temperature in our sol-gel process. Our method for preparing BFO nanoparticles allowed us to control the particle size. We were able to modify the BFO lattice parameters, and as a consequence, induce ferromagnetism in otherwise antiferromagnetic bulk BFO. To elucidate the origin of the ferromagnetic order in our NPs we performed DFT calculations using the BFO parameters obtained from experiment. We found that even small distortions of the structural lattice on the order of 0.01% modifies the relative angle of Fe–O–Fe ions, and therefore alters the energy bands. This induces a significant spin imbalance close to the Fermi energy on the Fe sites, increases the electronic gap, and results in a redistribution of the spin and charge within the unit cell. In addition, our calculations showed that the role of SOC in BFO may not be fundamental for the strain-induced magnetism reported here; however, the changes in the band structure in the NPs compared to the bulk indicate that changes in the Fe–O–Fe bond length due to lattice changes are more relevant. Finally, our results shed light on the appearance of the weak ferromagnetism in strained BFO thin films reported earlier and offers a new route to novel voltage-controlled spintronic devices based in multiferroic materials.

Acknowledgments

This work was initiated at the Nanomagnetism Laboratory at Universidad de los Andes. We acknowledge support from the FAPA program by means of Facultad de Ciencias and Vicerrectoria de Investigaciones of Universidad de los Andes, Bogotá, Colombia. Funds were also provided by the bilateral grant ‘Tec de Monterrey- Uniandes Program’ and Interdisciplinary grant. The authors acknowledge the Brazilian Nanotechnology National Laboratory (LNNano) for the use of the electron microscopy facility under the projects # 22424. DM acknowledges the Brazilian agencies FAPESP (2017/1058-1) and CNPq (303236/2017-5). ACR acknowledges support from the Facultad de Ciencias, Universidad de los Andes (2019-II). ER wants acknowledge support from Colciencias-Colfuturo

for supporting a doctoral scholarship through the 'Convocatoria Doctorados Nacionales No. 617, 2014-2'.

ORCID iDs

Juan Gabriel Ramirez https://orcid.org/0000-0001-8546-6966

References

[1] Cohen R E 1995 *Nature* **358** 136
[2] Cheng Z, Hong F, Jia T, Zhao H, Wang Z, Wang Y, Ozawa K and Kimura H 2019 *Nanoscale Ferroelectric-Multiferroic Materials for Energy Harvesting Applications* (New York: Elsevier) pp 23–39
[3] Haumont R, Bouvier P, Pashkin A, Rabia K, Frank S, Dkhil B, Crichton W, Kuntscher C and Kreisel J 2009 *Phys. Rev.* B **79** 184110
[4] Huang C and Chen L 2014 *Materials* **7** 5403
[5] H'Mok H L, Martínez Aguilar E, Antúnez García J, Ribas Ariño J, Mestres L, Alemany P, Galván D H, Siqueiros Beltrones J M and Raymond Herrera O 2019 *Comput. Mater. Sci.* **164** 66
[6] Varignon J, Bibes M and Zunger A 2019 *Nat. Commun.* **10** 1658
[7] Spaldin N A and Fiebig M 2005 *Science* **309** 391
[8] Ramesh R and Spaldin N A 2007 *Nat. Mater.* **6** 21
[9] Bibes M and Barthélémy A 2008 *Nat. Mater.* **7** 425
[10] Zhang J T, Lu X M, Zhou J, Sun H, Su J, Ju C C, Huang F Z and Zhu J S 2012 *Appl. Phys. Lett.* **100** 242413
[11] Dutta D P, Jayakumar O D, Tyagi A K, Girija K G, Pillai C G S and Sharma G 2010 *Nanoscale* **2** 1149
[12] Dutta D P, Mandal B P, Naik R, Lawes G and Tyagi A K 2013 *J. Phys. Chem.* C **117** 2382
[13] Park T-J, Papaefthymiou G C, Viescas A J, Moodenbaugh A R and Wong S S 2007 *Nano Lett.* **7** 766
[14] Kubel F and Schmid H 1990 *Acta Crystallogr.* B **46** 698
[15] Sosnowska I and Zvezdin A K 1995 *J. Magn. Magn. Mater.* **140–4** 167
[16] Tabares-Mun˜oz C, Rivera J-P, Bezinges A, Monnier A and Schmid H 1985 *Japan. J. Appl. Phys.* **24** 1051
[17] Catalan G and Scott J F 2009 *Adv. Mater.* **21** 2463
[18] Park J-G, Le M D, Jeong J and Lee S 2014 *J. Phys.: Condens. Matter* **26** 433202
[19] Carranza-Celis D, Cardona-Rodríguez A, Narváez J, Moscoso-Londono O, Muraca D, Knobel M, Ornelas-Soto N, Reiber A and Ramírez J G 2019 *Sci. Rep.* **9** 3182
[20] Ederer C and Spaldin N A 2005 *Phys. Rev.* B **71** 060401
[21] Huang F *et al* 2013 *Sci. Rep.* **3** 2907
[22] Yaakob M K, Taib M F M, Deni M S M, Chandra A, Lu L and Yahya M Z A 2013 *Ceram. Int.* **39** S283
[23] Fujita K and Gohda Y 2019 *Phys. Rev. Appl.* **11** 024006
[24] Hasan M, Islam M F, Mahbub R, Hossain M S and Hakim M A 2016 *Mater. Res. Bull.* **73** 179
[25] Doebelin N and Kleeberg R 2015 *J. Appl. Crystallogr.* **48** 1573
[26] Kresse G and Furthmüller J 1996 *Phys. Rev.* B **54** 11169
[27] Perdew J P, Burke K and Ernzerhof M 1996 *Phys. Rev. Lett.* **77** 3865
[28] Khorsand Zak A, Abd Majid W H, Abrishami M E and Yousefi R 2011 *Solid State Sci.* **13** 251
[29] Hoshina T, Wada S, Kuroiwa Y and Tsurumi T 2008 *Appl. Phys. Lett.* **93** 192914
[30] Mendoza Zélis P, Muraca D, Gonzalez J S, Pasquevich G A, Alvarez V A, Pirota K R and Sánchez F H 2013 *J. Nanoparticle Res.* **15** 1613
[31] Xu B, Dupé B, Xu C, Xiang H and Bellaiche L 2018 *Phys. Rev.* B **98** 18
[32] Blöchl P E 1994 *Phys. Rev.* B **50** 17953
[33] Béa H, Gajek M, Bibes M and Barthélémy A 2008 *J. Phys.: Condens. Matter* **20** 434221
[34] Ramírez-Camacho M C, Sánchez-Valdés C F, Gervacio-Arciniega J J, Font R, Ostos C, Bueno-Baques D, Curiel M, Sánchez-Llamazares J L, Siqueiros J M and Raymond-Herrera O 2017 *Acta Mater.* **128** 451
[35] Dixit H, Hee Lee J, Krogel J T, Okamoto S and Cooper V R 2015 *Sci. Rep.* **5** 12969
[36] Kan D and Takeuchi I 2010 *J. Appl. Phys.* **108** 014104
[37] Waterfield Price N, Vibhakar A M, Johnson R D, Schad J, Saenrang W, Bombardi A, Chmiel F P, Eom C B and Radaelli P G 2019 *Phys. Rev. Appl.* **11** 024035
[38] Martin L W, Crane S P, Chu Y-H, Holcomb M B, Gajek M, Huijben M, Yang C-H, Balke N and Ramesh R 2008 *J. Phys.: Condens. Matter* **20** 434220